



In situ interlayer hot forging arc plasma directed energy deposition of Inconel® 625: microstructure evolution during heat treatments



Francisco Werley Cipriano Farias^{a,*}, Valdemar R. Duarte^{a,b}, Igor Oliveira Felice^a, João da Cruz Payão Filho^c, Norbert Schell^d, Emad Maawad^d, J.Y. Li^e, Y. Zhang^e, T.G. Santos^{a,b}, J.P. Oliveira^{a,f,**}

^a UNIDEMI, Department of Mechanical and Industrial Engineering, NOVA School of Science and Technology, Universidade NOVA de Lisboa, 2829-516 Caparica, Portugal

^b Laboratório Associado de Sistemas Inteligentes, LASI, 4800-058 Guimarães, Portugal

^c Program of Metallurgical and Materials Engineering, Federal University of Rio de Janeiro (UFRJ), CEP 21941-972 Rio de Janeiro, RJ, Brazil

^d Helmholtz-Zentrum Hereon, Institute of Materials Physics, Max-Planck-Str. 1, Geesthacht, Germany

^e Herbert Gleiter Institute of Nanoscience, School of Materials Science and Engineering, Nanjing University of Science and Technology, Nanjing 210094, China

^f CENIMAT|3N, Department of Materials Science, School of Science and Technology, NOVA University Lisbon, Caparica, Portugal

ARTICLE INFO

Article history:

Received 10 February 2023

Received in revised form 24 March 2023

Accepted 8 April 2023

Available online 11 April 2023

Keywords:

Wire and arc additive manufacturing

Directed energy deposition

Ni-based superalloys

Inconel 625

Synchrotron X-ray diffraction

ABSTRACT

The study reports that the combined use of *in situ* interlayer hot forging and post-deposition heat treatment (PDHT) could alter the typical coarse and oriented microstructure of the Ni-based superalloy 625 obtained by arc plasma directed energy deposition (DED) to a fine and non-oriented condition. *In situ* synchrotron X-ray diffraction and electron backscatter diffraction showed that the high-temperature (1100 °C/ 1 h) PDHT induced significant recrystallization, leading to grain refinement and low texture index, while partially dissolving deleterious Laves and δ phases. Low-temperature (980 °C/ 1 h) PDHT had a limited effect on the grain size refinement and induced the formation of secondary phases. It is shown that conventional heat treatments applied to Ni-based superalloy 625 obtained by arc plasma DED are not conducive to optimized microstructure features. *In situ* hot forging induced enough crystal defects to promote static recrystallization during PDHT. Besides, high-temperature PDHT met the AMS 5662 grain size requirements.

© 2023 The Author(s). Published by Elsevier B.V. This is an open access article under the CC BY-NC-ND license (<http://creativecommons.org/licenses/by-nc-nd/4.0/>).

1. Introduction

Ni-based superalloys (e.g., Inconel® 625 and 718) fabricated via fusion-based additive manufacturing (AM) processes (e.g., directed energy deposition – DED, ISO/ASTM 52900) typically possess a coarse and oriented microstructure with intense interdendritic segregation, which results in anisotropic and inferior mechanical properties, low heat treatment response, and poor corrosion resistance [1–9]. To overcome these process limitations, strategies to refine the grain size have been developed, e.g., using inoculants, ultrasound vibration, thermal management, magnetic field stir, and interlayer deformation [10–15]. The latter stands out for refining the grain size through *in situ* and *ex situ* recrystallization mechanisms

without affecting the material specification (chemical composition) and deposition process conditions. Among interlayer deformation processes, it can distinguish the rolling and hammer/peening/forging, which were classified by the temperature (cold – below – and hot – above the recrystallization temperature, respectively) and deformation mode (almost homogeneous and quasi-static – rolling – and localized and dynamic – peening/hammering/forging) [16].

The interlayer deformation was first used to enhance the fatigue life of weldments and improve weldability [17–20]. However, given the intricate 3D part geometries related to AM, these previously developed deposition + interlayer deformation systems were not used due to the path planning limitations, which demanded the development of dedicated tools to be applied to the AM field. In addition, even the dedicated (hot and cold) rolling interlayer deformation systems developed for AM showed path planning limitations [21], which may hinder its industrial scalability, highlighting the hammer/peening/forging interlayer deformation systems by the ability to be coupled to robotic arms [14]. Additionally, alloys fabricated by arc plasma DED (e.g., AISI 316 L stainless steel [22], Inconel® 718 [23,24], and Al series 2xxx [25]) had suitable workability,

* Corresponding author.

** Corresponding author at: UNIDEMI, Department of Mechanical and Industrial Engineering, NOVA School of Science and Technology, Universidade NOVA de Lisboa, 2829-516 Caparica, Portugal.

E-mail addresses: fw.farias@campus.fct.unl.pt (F.W.C. Farias), j.p.oliveira@fct.unl.pt (J.P. Oliveira).

which supports the promising use of the DED + interlayer (cold or hot) deformation systems.

Zhao et al. [26] and Li et al. [27] applied hot interlayer deformation during laser-DED of solid-solution strengthened Ni-based superalloys (Ni 60 and Ni80-Cr20, respectively). These authors reported a less oriented microstructure, higher hardness, and low wear rate in relation to conventionally processed laser-DED counterparts. Precipitation-strengthened Ni-based superalloys (Inconel® 718) fabricated via DED + interlayer deformation showed a remarkable grain size refinement (static recrystallization) during the mandatory post-deposition heat treatment (PDHT, e.g., solution + double-aging) [15,28–30], which resulted in grain size and quasi-static mechanical properties similar to that of wrought material (meeting the AMS 5662 grain size requirement). In addition, Farias et al. [31] demonstrated the beneficial synergic action of the in situ interlayer hot forging and PDHT to refine the grain size of the Inconel® 625 fabricated via arc plasma DED; however, the microstructure evolution over the PDHT soaking time has not been elucidated.

Thus, given the typical columnar coarse grain and highly textured microstructure of Inconel® 625 obtained by arc plasma DED [1–8] and the grain size refinement induced by the interlayer deformation and PDHT observed for Inconel® 625 [31] and 718 [14–16,28–30,32], the present work evaluates the microstructure evolution during the standard PDHTs (980 and 1100 °C/ 1 h) of the of Inconel® 625 fabricated via in situ interlayer hot forging arc plasma DED using in situ synchrotron X-ray diffraction (SXRD) and *ex situ* electron backscatter diffraction (EBSD).

2. Materials and methods

The in situ hot forging arc plasma DED 3D printer, which was in-house developed, [14,33] consisted of a KEMPY PRO MIG 3200 welding and 3-axis CNC machines, which was used to deposit the Inconel® 625 (AWS A5.14 ERNiCrMo-3; 1.2 mm) single-bead multi-layer walls on ASTM A36 Q235 steel plates. Fig. 1 and Table 1 detail the in situ interlayer hot forging system and deposition parameters, respectively. Fig. 2 depicts the macroscopical aspects of the in situ interlayer hot forging arc plasma DED of Inconel® 625, highlighting the flat layer surface and typical part waviness, which showed the process's suitability to print medium to large metal parts. For more details on the in situ interlayer hot forging process, the readers are referred to Duarte et al. [14,33] and Farias et al. [31].

PDHT usually do not alter the grain size and morphology of Ni-based superalloys obtained by arc plasma DED [1,2,29,30,3–8,15,28]. Thus, the effect of conventional heat treatments applied to Inconel® 625 was evaluated in an in situ interlayer hot forging arc plasma DED counterpart. PDHTs (Fig. 3a), solution (1100 °C/1 h) and stabilization (980 °C/1 h), conditions were selected based on the Inconel® 625 wrought material specification (ASTM B 446). *In situ* SXRD (HEMS beamline of PETRA III/DESY, Hamburg, Germany) was executed during the PDHT schedules (Fig. 3b details the experimental apparatus). SXRD acquisition rate, exposure time, wavelength, and spot size (area covered by the X-ray beam) were 0.25 Hz, 4 s, 0.14235 Å, and 1 × 1 mm², respectively. The 2D Debbye-Scherrer diffraction rings were post-processed in Fit2D [34] and followed the Rodriguez et al. [35,36] procedure.

After PDHTs (*ex situ*), the final grain size (measured using the intercept method – following ASTM E112) and crystallographic orientation (represented by pole figures and orientation distribution function – ODF using the Bunge notation) were evaluated through large EBSD maps (1.95 × 1.95 mm²; Fig. 3c), which were obtained from in the interlayer region (between the 7th and 8th layers). The EBSD data post-processing was performed using the MTEX toolbox [37].

3. Results and discussion

3.1. Post-deposition heat treatment (PDHT) – *Ex situ* EBSD

Fig. 4 summarizes the effect of the PDHTs on Inconel® 625 fabricated via in situ interlayer hot forging arc plasma DED. Three distinct regions can be observed: (1) fine grain size region, which originated from the in situ dynamic recrystallization (hot forging effect); (2) static (*ex situ*) recrystallized region (PDHT effect); and (3) unchanged columnar grains, resulting from the primary solidification microstructure. As described by Duarte et al. [14,33], the direct forging on the incandescent just deposited material (~ 900 – 1100 °C) induces dynamic recrystallization, leading to a fine and equiaxed grain structure at the layer top surface. The rest of the layer, where in situ dynamic recrystallization does not occur, still possesses remaining deformation due to the in situ interlayer hot forging. The remaining deformation can drive static recrystallization during PDHT (as observed in region (2)), characterizing a double grain size refinement mechanism (in situ and *ex situ*), as verified in our previous work [31] and also proposed by Wang and Shi [39] (Inconel® 718 fabricated via in situ interlayer ultrasonic impact peening laser-DED). However, due to the higher layer height (4 – 6 mm) of the arc plasma DED in relation to laser-DED [29,39], the hot forging deformation does not affect the whole layer, i.e., a primary microstructure (region (3), refer to Fig. 4) persists.

Region (1) had an almost similar extension and grain size in both PDHTs, 24.19 ± 6.1 and 39.11 ± 11.4 μm for the solution and stabilization conditions, respectively. This was expected since region (1) rose from the hot forging process. In addition, static recrystallization (during PDHT) can also occur in the region (1), which explains the finer grain size of the solution PDHT condition. Region (2) diverged significantly between PDHTs, especially in extension (~ 950 vs. 440 μm for solution and stabilization, respectively). In addition, the average grain size of the solution PDHT was finer than the stabilization one (56.57 ± 32.1 vs. 74.03 ± 25.9 μm). Also, the solution PDHT (ASTM E112 grain size No. 5) accomplished the AMS 5662 and API 6A718 grain size requirements (ASTM E112 grain size No. ≥ 5 and ≥ 3, respectively), showing that the in situ interlayer hot forging arc plasma DED industrial suitability. Due to the lower deformation induced during the deposition process in relation to laser-based additive manufacturing processes, Ni-based superalloys fabricated via arc plasma DED did not present evidence of static recrystallization during the typical PDHT [5,6,15,40–45], which prevents grain size refinement via static recrystallization (i.e., maintaining the coarse and oriented columnar grains) and, consequently, limits the use of Ni-based superalloys fabricated via arc plasma DED in mission-critical applications (not meeting the rigid materials requirements, e.g., oil & gas – API 6A718 – and aviation – AMS 5662 – industries). The present work shows that the coarse grain size challenge observed for Ni-based alloys fabricated via arc plasma DED can be overcome using the in situ interlayer hot deformation followed by an adequate PDHT (1100 °C/ 1 h).

The effect of PDHT peak temperature (980 and 1100 °C) can be related to the driving force for recrystallization since a higher temperature increases the transformation kinetics and induces deeper recrystallization through the layer height (the deformation induced by hot forging is higher closer to the layer top surface). This can be verified by the kernel average misorientation (KAM) maps, which demonstrate that the stabilization PDHT had higher KAM than the solution PDHT condition, i.e., the stabilization PDHT did not promote a complete recrystallization in all regions, failing to relieve the remaining deformation induced by the in situ interlayer hot forging. Despite the Inconel® 625 obtained by arc plasma DED does not have a mandatory PDHT, in situ grain size refinement (via dynamic recrystallization, i.e., interlayer hot forging effect) is insufficient to change the as-built microstructure noticeably, as previously

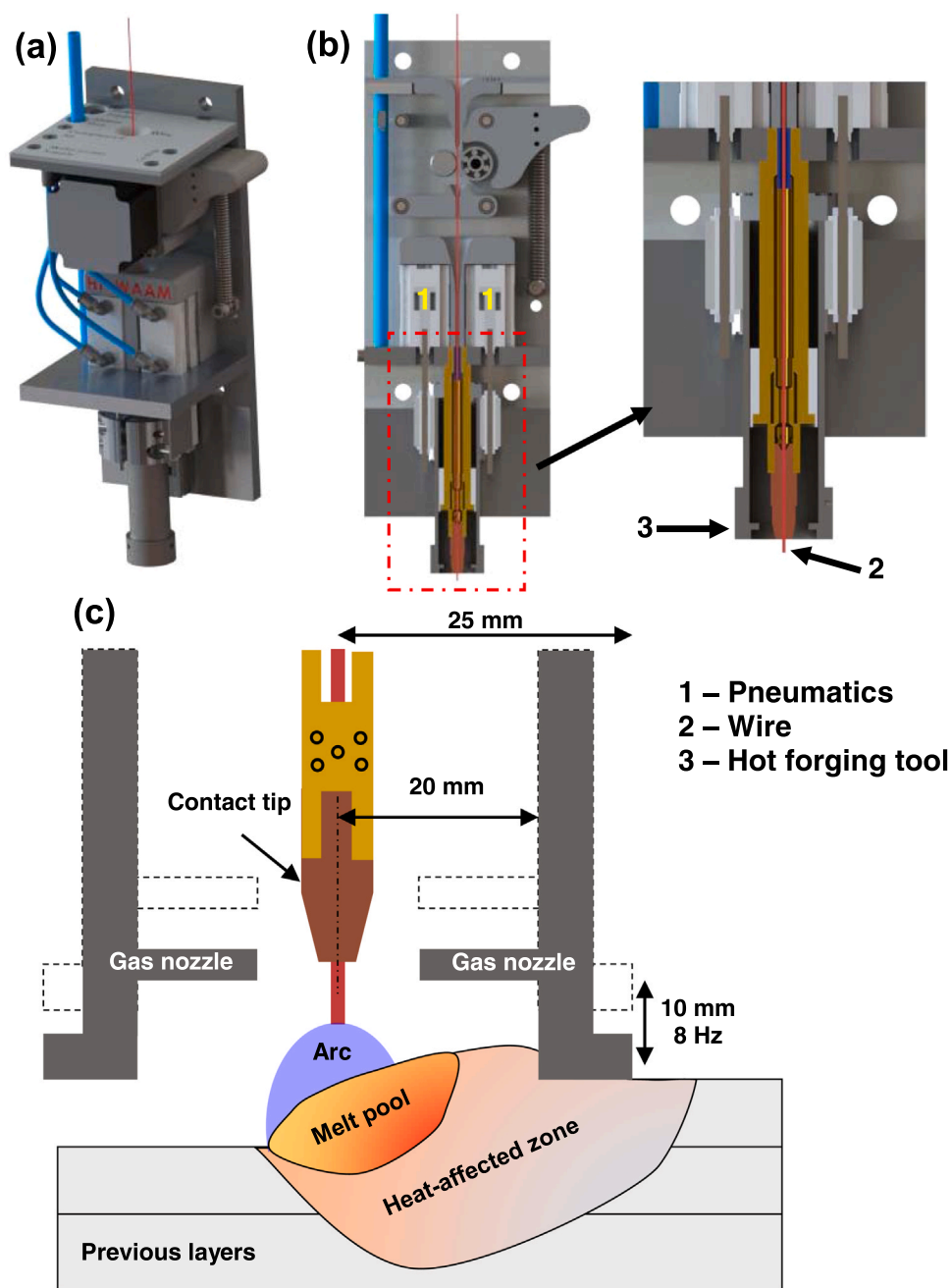


Fig. 1. *In situ* interlayer hot forging arc plasma DED system: (a) isometric view and (b) cross-section details. (c) Schematic representation of the deposition process.

Table 1

In situ interlayer hot forging arc plasma DED parameters.

Arc plasma DED	
Electric current*	72.1 [A]
Arc voltage*	17.1 [V]
Wire feed speed	3.5 [m/min]
Travel speed	5.0 [mm/s]
Heat input†	209.6 [J/mm]
Idle time	90 [s]
CTWD‡	10 [mm]
Shielding gas/flow	Ar/15 l/min
Hot forging	
Pneumatic pressure	500 [kPa]
Frequency	8 [Hz]

* Root-mean-square

‡ Contact tip to work distance

† Thermal efficiency ($\eta = 0.85$) [38]

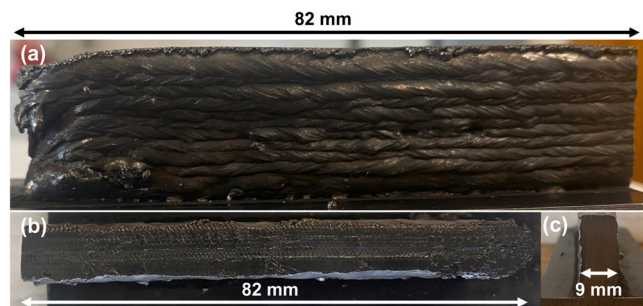


Fig. 2. Macroscopic aspects of the in situ interlayer hot forging arc plasma directed energy deposition of Inconel® 625: (a) side view, (b) top view, and (c) cross-section of a single-bead multi-layer 3D printed part.

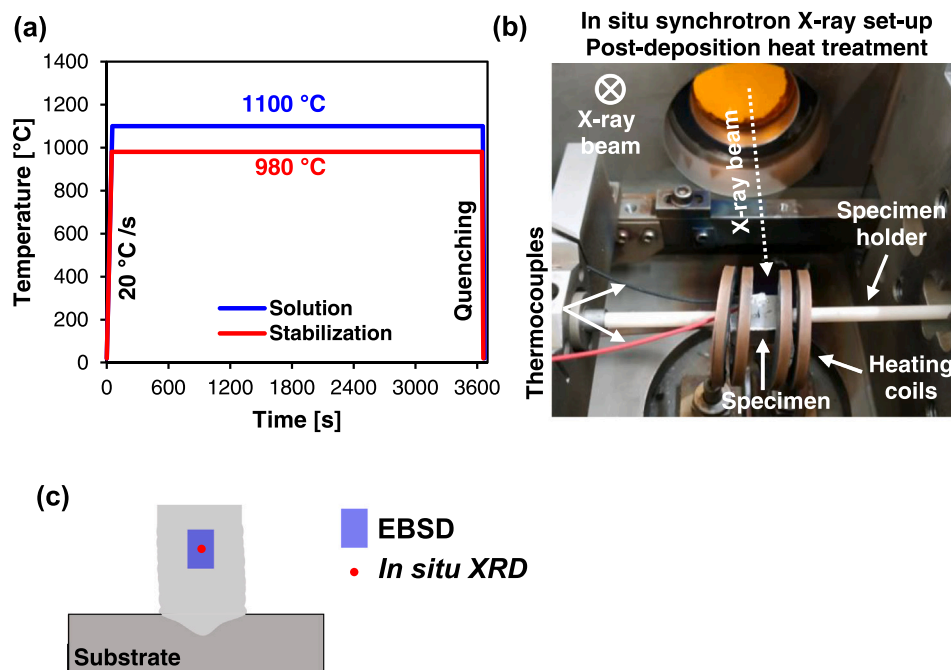


Fig. 3. (a) Solution and stabilization post-deposition heat treatments (PDHT), (b) in situ SXRD and PDHT set-up, and (c) location in the sample where the EBSD and in situ SXRD analyses were performed.

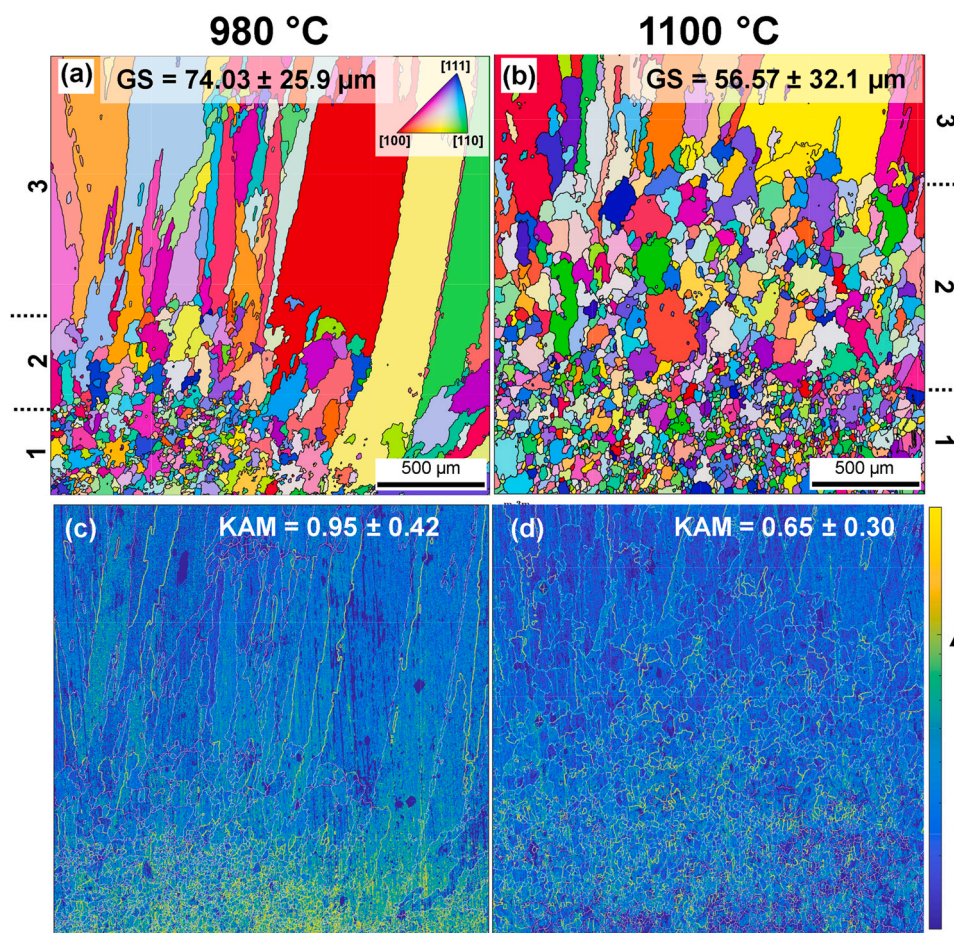


Fig. 4. Ex situ EBSD analysis. Stabilization (980 °C/1 h) PDHT: (a) image orientation map (IOM) and (c) kernel average misorientation (KAM). Solution (1100 °C/1 h) PDHT: (b) IOM and (d) KAM. GS mean grain size.

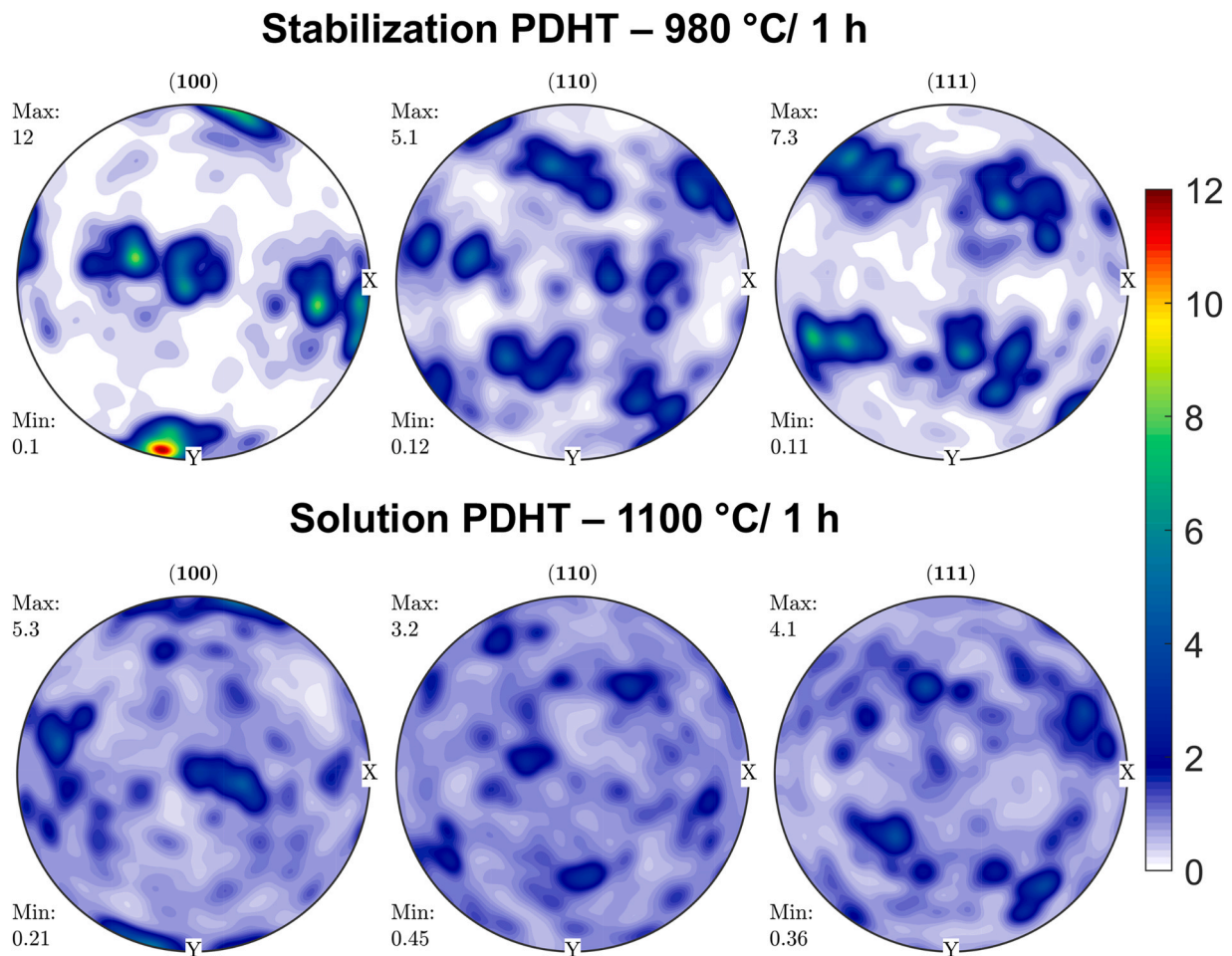


Fig. 5. Pole figure of the Inconel® 625 fabricated via in situ interlayer hot forging arc plasma directed energy deposition after stabilization (980 °C/ 1 h) and solution (1100 °C/ 1 h) PDHT.

reported by Farias et al. [31], Zhao et al. [26], and Li et al. [27] (solid-solution strengthened Ni-based superalloys fabricated via interlayer deformation DED), reinforcing the synergic effect of in situ interlayer hot forging (induce enough crystal defects) and selected PDHT (drive static recrystallizing) in promoting a significant grain size refinement.

As a consequence of the *ex situ* static recrystallization during the PDHT, the crystallographic texture (Fig. 5, Fig. 6, and Fig. 7) also depends on the PDHT peak temperature. The pole figures (Fig. 5) show that the stabilization PDHT did not alter the typical cube texture ($\{100\} \langle 100 \rangle$) aspect of the Ni-based superalloys obtained via arc plasma DED [1–8]. The finer grains (regions (1) and (2)) had an almost random-oriented microstructure (Fig. 6 and Fig. 7); thus, as the solution PDHT promoted a significant grain refinement, its general texture (regions (1), (2), and (3)) had a non-oriented aspect. Due to the minor extension of the region (2), the stabilization PDHT did not significantly alter the coarse and oriented microstructure, maintaining the cube texture. In addition, it is worth mentioning that the flat layer surface induced by the hot forging (Fig. 2) can alter the melt pool morphology, i.e., the in situ interlayer hot forging can promote a melt pool with a flatter penetration aspect in relation to arc plasma DED (finger-like penetration with a concave aspect), tilting the grain growth direction in relation to melt pool center and promoting some rotated cube texture aspects (e.g., $\{100\} \langle 1\bar{3}0 \rangle$), as reported by Gustafsson et al. [46] (Inconel® 625 welded) and Moat et al. [47] (Waspaloy® fabricated via laser-DED).

Therefore, in situ interlayer hot forging was able to induce static recrystallization during the PDHT and alter the microstructure of the

Inconel® 625 fabricated by arc plasma DED, changing the coarse and oriented columnar grains to fine equiaxed and non-oriented ones, eliminating the typical cube texture of fusion-based processed Ni-based superalloys (e.g., laser-DED, arc plasma-DED, PBF, welding, and casting).

3.2. Time-solved SXRD

3.2.1. In situ dislocation density estimation

The evolution of the full width at half maximum (FWHM) during the PDHT was tracked through the in situ SXRD (Fig. 8a). Peak broadening is affected by crystallite size (D), microstrain (ϵ , e.g., nonuniform strain, subgrains, and dislocations), and system configuration (e.g., instrument, material, and wavelength) [49,50]. Given the similar deposition conditions and SXRD configuration, the main difference between the solution and stabilization PDHTs can be related to microstrain evolution. In addition, subgrain formation and high-angle grain boundary migration decrease the crystal defects density [51–53], i.e., the diffraction peak broadening sources density should reduce along the PDHT's soaking time. Thus, the FWHM can qualitatively estimate the restoration phenomena during heat treatments [54]. In addition, the dislocation distribution and density of a deformed material are related to its SFE. A low/medium SFE material (e.g., Ni-based superalloys) possesses a low dislocation mobility due to the higher distance between partial dislocations, which hinder their constriction, i.e., the dislocation cross-slip and climb phenomena are harder to occur. Otherwise, high SFE materials have a low distance between partial dislocations, which promotes

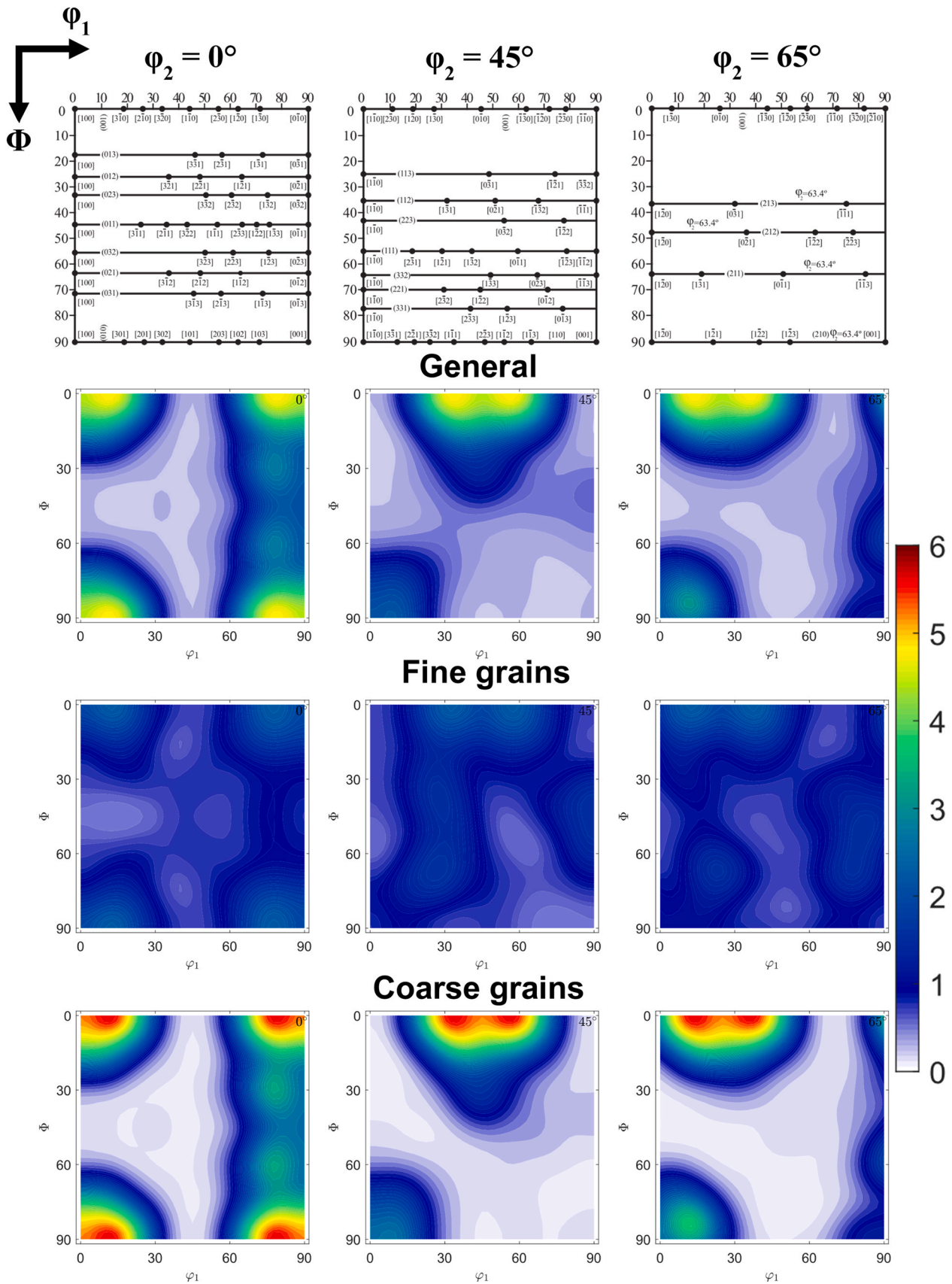


Fig. 6. Orientation distribution function (ODF) of the in situ interlayer hot forging arc plasma directed energy deposition of Inconel® 625 obtained by arc plasma DED after stabilization PDHT (980 °C/ 1 h). Constant- ϕ_2 sections (0, 45, and 65°) through the Eulerian space (Bunge [48]). The general ODFs, refined grains ODFs, and coarse grains ODFs refer to regions (1, 2, and 3), regions (1 and 2), and region (3) in Fig. 4a.

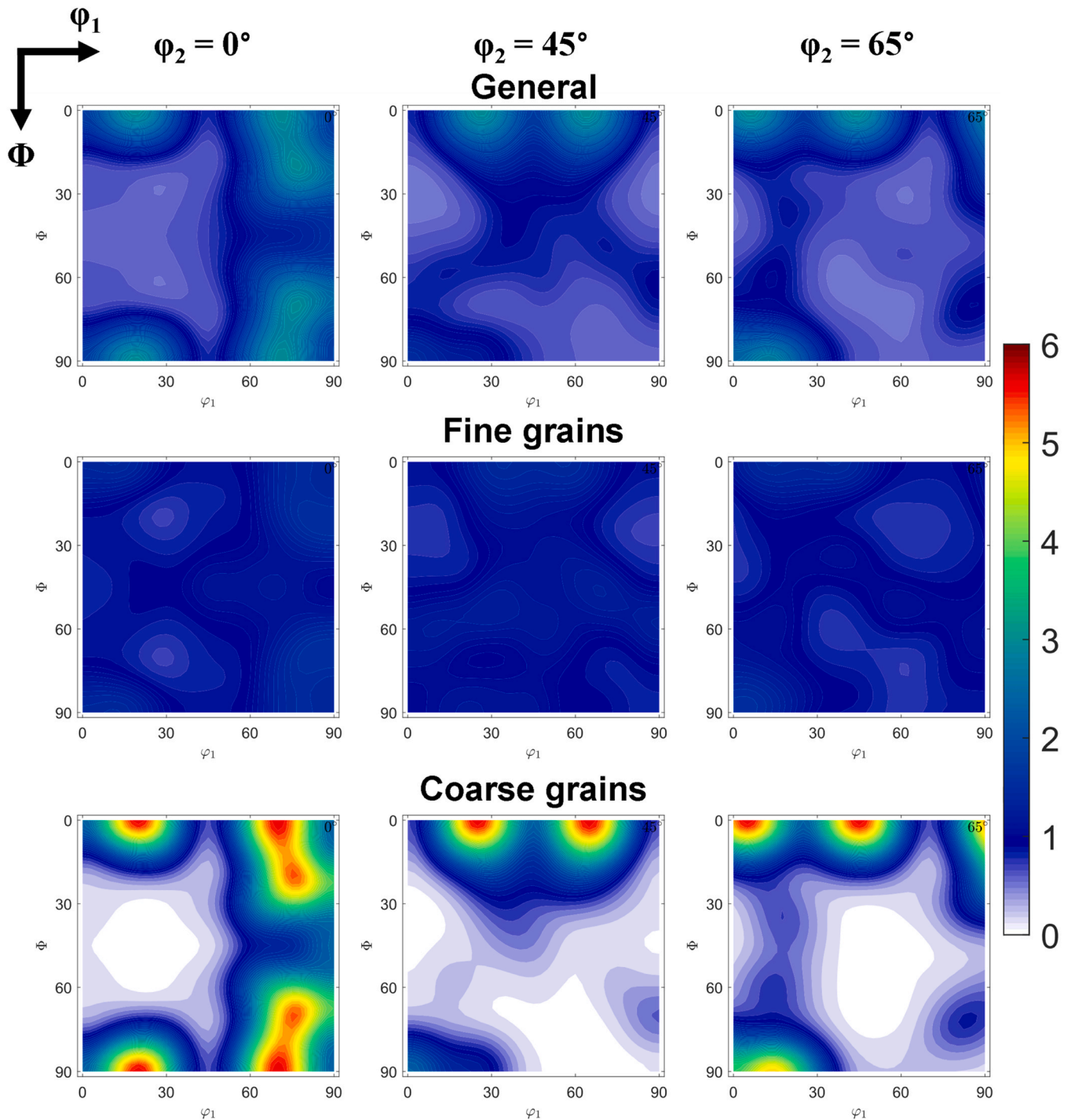


Fig. 7. Orientation distribution function (ODF) of the in situ interlayer hot forging arc plasma directed energy deposition of Inconel® 625 obtained by arc plasma DED after solution PDHT (1100 °C/ 1 h). Constant- ϕ_2 sections (0, 45, and 65°) through the Eulerian space (Bunge [48]). The general ODFs, refined grains ODFs, and coarse grains ODFs refer to regions (1, 2, and 3), regions (1 and 2), and region (3) in Fig. 4b.

the recovery phenomenon (dislocation migration and annihilation) since the dislocation mobility is facilitated (dislocation cross-slip and climb) [55,56]. Argon and Moffatt [57] proposed that the recovery rate is proportional to SFE^2 . Consequently, for low/medium SFE materials, slight dislocation recovery tends to occur before recrystallization. Thus, considering the low/medium SFE (20 – 30 $\text{mJ}\cdot\text{m}^{-2}$) of Inconel® 625, recrystallization can be appointed as the dominant restoration phenomenon, i.e., the reduction of FWHM and dislocation density during PDHT can be associated with static recrystallization.

From Williamson and Hall [58] (Eq. 1) and Smallman and Westmacott [59] (Eq. 2), the dislocation density (ρ_s , statistically stored dislocations – Fig. 8b) can be related to the FWHM [60,61]. In addition, given the lattice parameter (a) and diffraction angle (θ ; Fig. 9a) evolution during the PDHT (e.g., dissolution, see Section 3.2.2), the burgers vector (b ; Fig. 9b) also changes over time. Thus, according to Bragg's law (Eq. 3) and the correlation between planar distance (d_{hkl}) and lattice parameters for cubic materials (Eq. 4), it is possible to correlate the diffraction data with the burgers vector (Eqs. 5 and 6). λ and α are the SXRD wavelength (0.14235 Å)

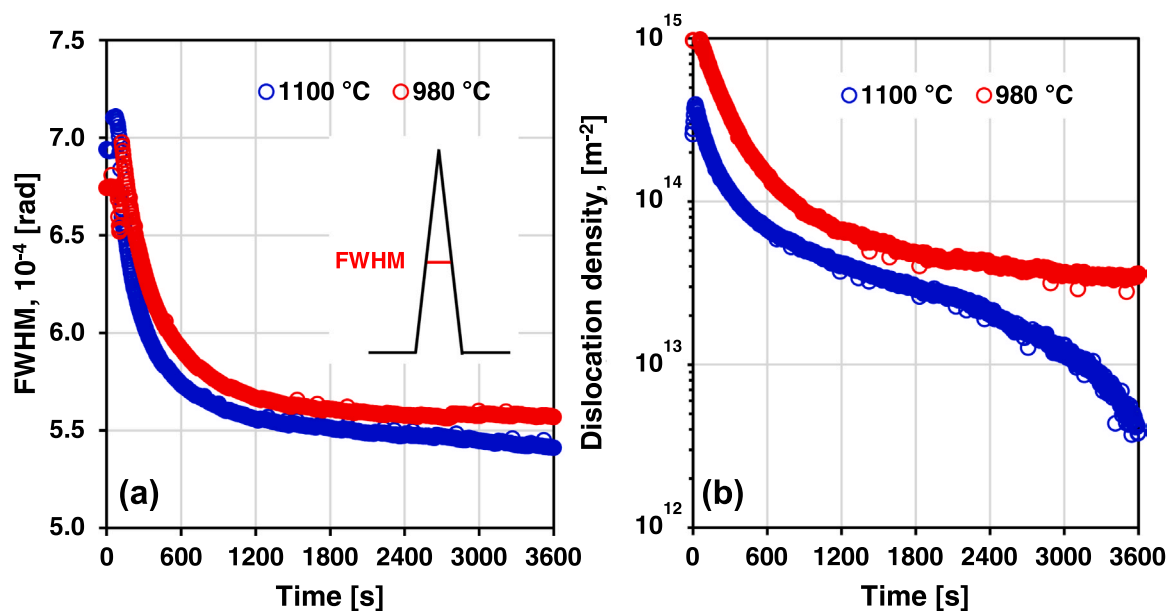


Fig. 8. Full width at half maximum (FWHM) and dislocation density evolution during solution (1100 °C) and stabilization (980 °C) PDHT.

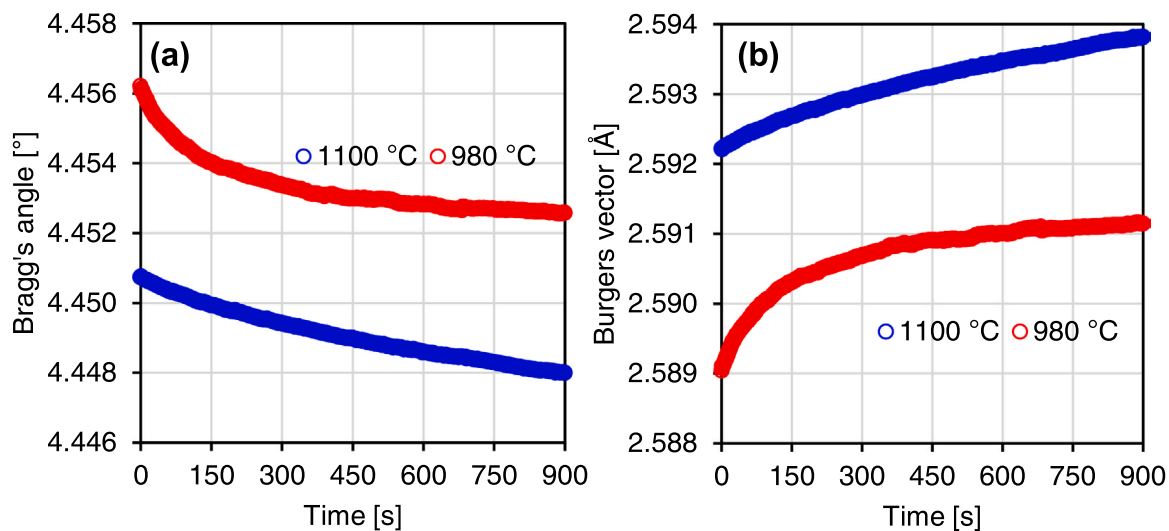


Fig. 9. Bragg's angle and Burgers' vector evolution during the stabilization (980 °C/1 h) and solution (1100 °C/1 h) post-deposition heat treatments.

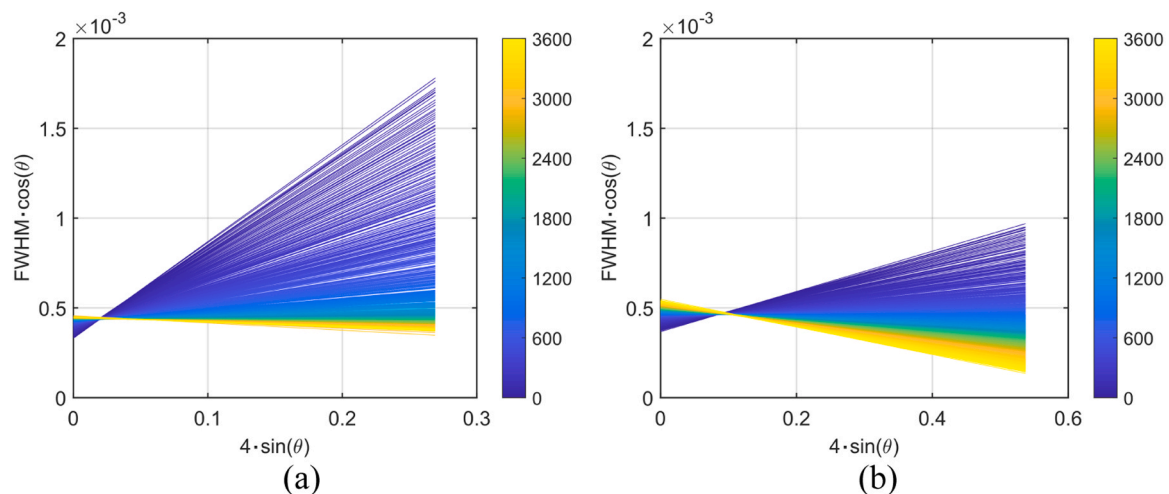


Fig. 10. Williamson-Hall plot for the (a) stabilization and (b) solution post-deposition heat treatments. The colorbar represents time evolution in seconds.

and the Scherrer factor of a cube-shaped crystallite (0.9), respectively. Therefore, ρ_s evolution can be estimated (Fig. 8b) from the Williamson-Hall plots (Fig. 10a and Fig. 10b), which were obtained in each 4 s during PDHTs.

$$FWHM \cdot \cos\theta = \frac{\alpha \cdot \lambda}{D} + 4 \cdot \sin\theta \cdot \varepsilon \quad (1)$$

$$\rho_s = \frac{16.1 \cdot \varepsilon^2}{b^2} \quad (2)$$

$$\lambda = 2d_{hkl} \sin\theta \quad (3)$$

$$d_{hkl} = \frac{a}{\sqrt{h^2 + k^2 + l^2}} \quad (4)$$

$$b = \frac{a}{\sqrt{2}}, \text{ FCC unit cell} \quad (5)$$

$$b = \frac{\lambda}{\sqrt{2} \cdot \sin\theta}, (200) \text{ plane} \quad (6)$$

Both PDHTs had a fast FWHM and dislocation density reduction in the first ~ 1200 s (20 min), which indicates that static recrystallization quickly occurs in the in situ interlayer hot forged material, as reported by Li et al. [62] (Inconel® 718 fabricated by in situ hot rolling laser-DED). After 1200 s, the stabilization PDHT reached a plateau in the FWHM evolution, meaning that the diffraction peak broadening sources stopped reducing, which evidenced a static recrystallization interruption. The solution PDHT showed a continuous drop in the FWHM after 1200 s, which is related to some recrystallization in the lower deformed grains (region (2)) and grain growth [63] during the remaining soaking time (~ 2400 s). Besides, abnormal secondary grain growth [45] was not observed (Fig. 4).

The recrystallization kinetics is associated with the deformation level (more deformed leading to faster kinetics) and temperature (higher temperature drives the recrystallization of less deformed regions) [64,65]. Thus, the solution PDHT can induce recrystallization in a larger area than the stabilization PDHT [63,66] since the localized and dynamic deformation aspects of hot forging cause a deformation gradient from the layer top surface [14,32,33]. In addition, the initial dislocation density ($\sim 4 \cdot 10^{14} \text{ m}^{-2}$ and $9 \cdot 10^{14} \text{ m}^{-2}$, refer to Fig. 8b) was similar in magnitude to Ni-based superalloys fabricated via powder bed fusion (PBF) ($\sim 4.9 - 9 \cdot 10^{14} \text{ m}^{-2}$) [63,67], which usually underwent static recrystallization during PDHT. Terris et al. [63] also verified a faster dislocation density reduction during the solution PDHT, which was also related to static recrystallization. Thus, the limited effect of PDHT on the grain size and crystallographic texture of the Inconel® 625 obtained by arc plasma DED [1,2,29,30,33–8,15,28] can be related to the low deformation level developed during the deposition (multiple thermal cycles), differing considerably from laser-based processes, which has higher deformation (driving force to recrystallization) levels due to the focused heat source and steeper cooling rates [12,66]. The in situ interlayer hot forging induced enough crystal defects and drove the static recrystallization of Inconel® 625 obtained by arc plasma DED during solution PDHT, which is typically not observed.

3.2.2. Secondary phase dissolution

Fig. 11 depicts the SXRD patterns and the evolution of the normalized peak intensity of the secondary phases (Laves and δ) identified in the present work. The diffraction patterns (Fig. 11a) of the solution and stabilization PDHTs did not have a notorious difference between them, indicating that their final microstructure had similar secondary phases. It is possible to observe less difference in the matrix (γ) peak intensities for solution PDHT due to the lower texture index and finer grain size (Fig. 4). In addition, the SXRD results are per DuPont et al. [68] (experimentally-based solidification model

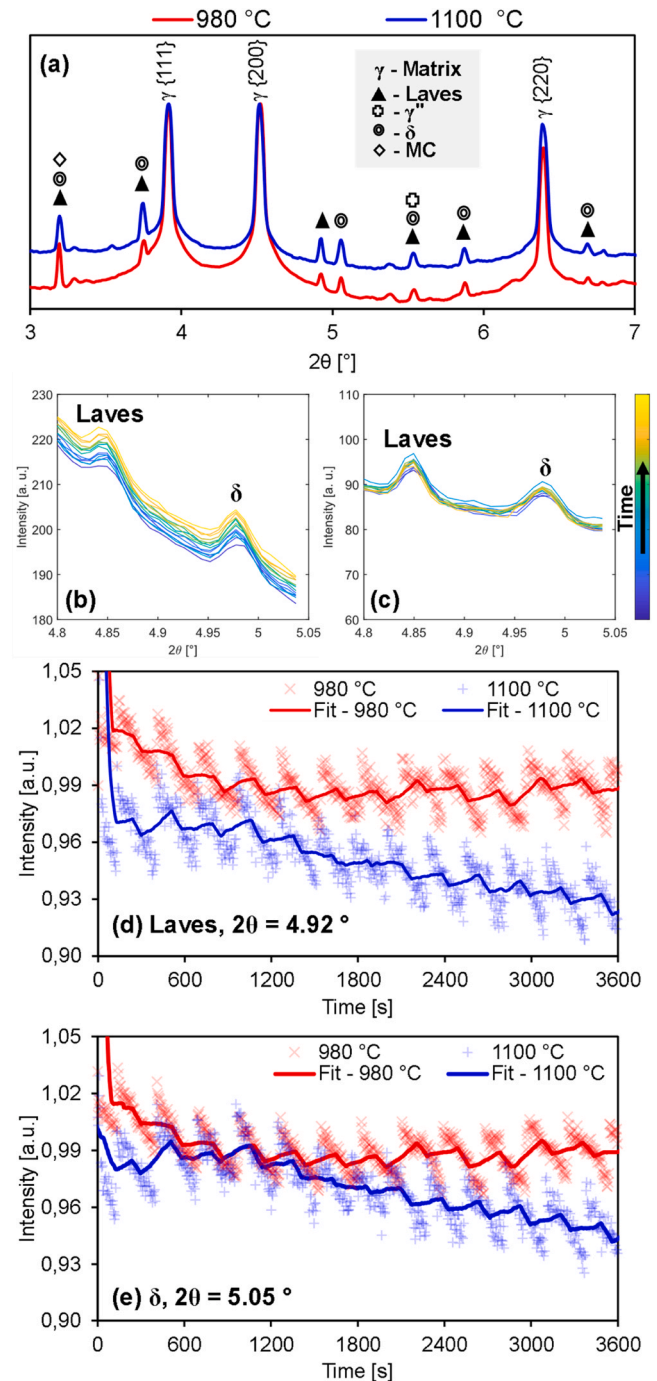


Fig. 11. SXRD analysis. (a) SXRD pattern, (b – c) Laves and δ phases isolated peaks evolution during the stabilization (980 °C) and solution (1100 °C) PDHTs, and (d – e) normalized peak intensity evolution. The fit function used in (d – e) is the moving mean.

for welding conditions) and Scheil–Gulliver model (Thermo-Calc®, Fig. 12a), which predicted the existence of Laves and MC-type carbides. σ and η phases (predicted by the Scheil–Gulliver model) are suppressed due to the higher ($\sim 10^2$ °C/s) [12,69] cooling rate (arc plasma DED vs. local equilibrium). These phases (σ and η) were also not observed by Schmeiser et al. [66] and Oh et al. [70], which also used in situ SXRD to characterize the Inconel® 625 fabricated via PBF. δ and γ'' phases originated from the multiple thermal cycles and PDHTs [6,66,71,72]. They were not associated with the solidification sequence experienced by the material despite the Scheil–Gulliver model (Fig. 12a) predicting δ phase formation during the

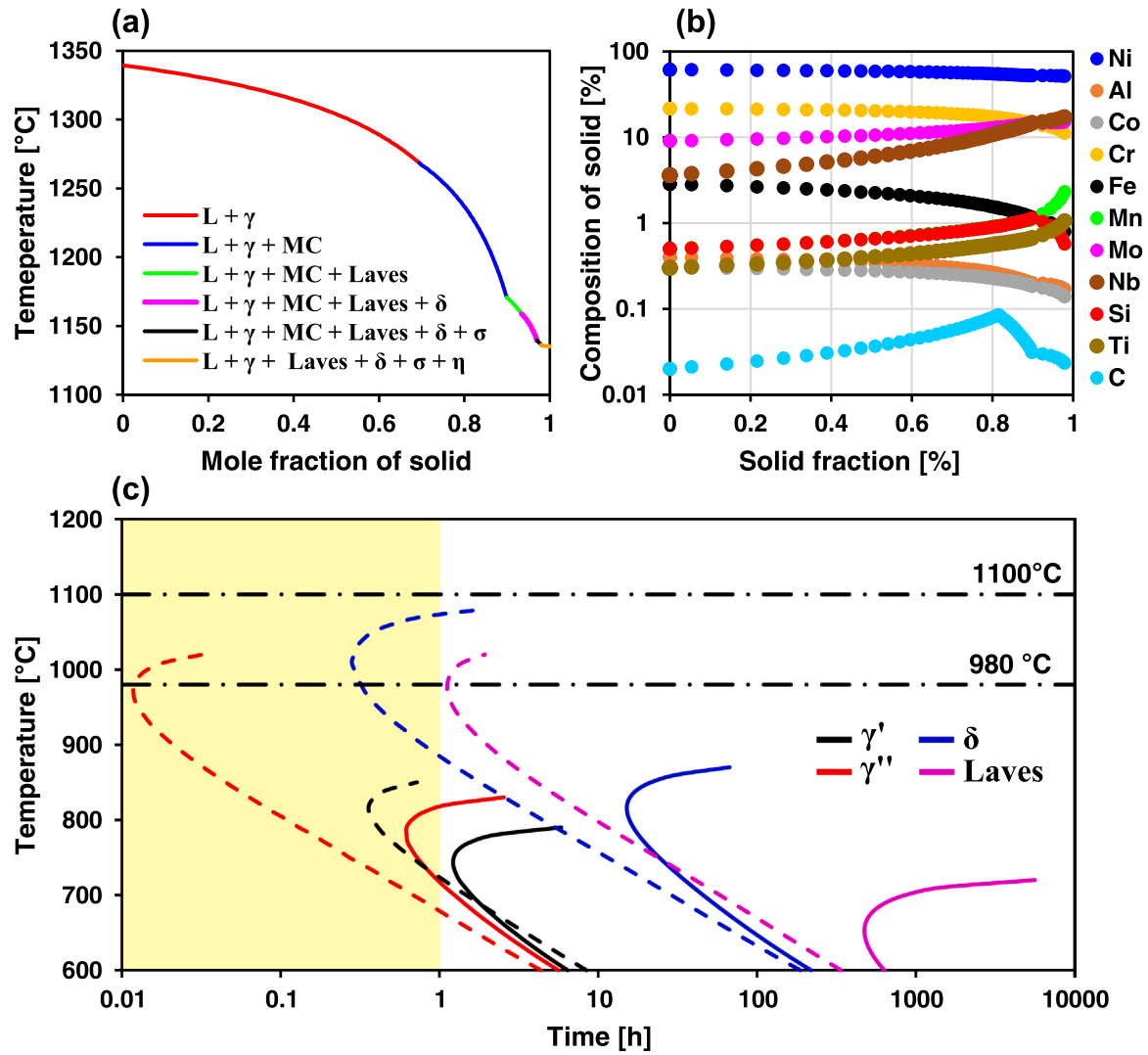


Fig. 12. (a) Inconel® 625 Scheil-Gulliver solidification model (Thermo-Calc®; TCNI11 database), (b) elemental distribution, and (c) transformation-time-temperature (TTT) diagram (JMatPro®) considering the dendritic core (solid line) and interdendritic region (dotted line) chemical compositions.

solidification sequence, which was also not experimentally observed by Oh et al. [70] (melting pool solidification characterized by in situ SXRD) and Cieslak [73,74] (differential thermal analysis).

Stabilization PDHT increased the Laves and δ phases peak intensity (Fig. 11b and Fig. 11c). In opposition, the solution PDHT first causes a slight increase and then a drop in peak intensity. These results are corroborated by the time-transformation-temperature (TTT) diagram (obtained with JMatPro®, Fig. 12c), which was calculated from the Scheil-Gulliver model chemical composition distribution (Thermo-calc®; Fig. 12b). During the stabilization PDHT, Laves and δ are stable in the interdendritic region, supporting the present in situ SXRD and literature results [6,69,72,75–80]. For the solution PDHT, Laves and δ are unstable, both in the interdendritic region and dendritic core, and should dissolve. However, their peak intensity increases initially, which can be related to local fast precipitation kinetics at the interdendritic region due to the higher Nb segregation (up to 25% wt.), as experimentally verified by Antonsson and Fredriksson [81].

Given the theoretical peak intensity (Eq. 7) and its correlation with phase volume in a multi-phase material diffractogram (Eq. 8; phases observed in the manuscript – Fig. 11a), the normalized data (Fig. 11d and Fig. 11e) of a single-phase diffraction peak (Eqs. 9, 10, and 11) can indicate the variation of phase content ($c(t)$) in relation the initial one (as-built condition, $c(0)$) [49]. I_{hkl} , I_0 , μ_0 , μ , M , e , A , and

r are the integrated intensity, intensity of the incident beam, $4\pi \cdot 10^{-7}$ m·kg·C⁻², linear absorption coefficient, temperature factor (Debye-Waller), charge on electron, cross-sectional area of incident beam, and radius of diffractometer circle, respectively. Given that the sample-detector (2D Perkin Elmer) was kept constant (1561.85 mm), μ not affected the relative values of I_{hkl} (Eq. 11) [82].

$$I_{hkl} = \left(\frac{I_0 A \lambda^3}{32 \pi r} \right) \left(\frac{\mu_0 e^2}{4 \pi m} \right)^2 \frac{1}{v^2} \left[F |hkl|^2 p \left(\frac{1 + \cos^2 2\theta}{\sin^2 \theta \cos \theta} \right) \right] \left(\frac{e^{-2M}}{2\mu} \right) \quad (7)$$

$$I_{hkl} = KR(\theta) \left(\frac{e^{-2M}}{2\mu} \right) (c_\gamma + c_{\gamma''} + c_\delta + c_{Laves} + c_{MC}) \quad (8)$$

$$I_{single-phase} = KR(\theta) \left(\frac{e^{-2M}}{2\mu} \right) c_{single-phase} \quad (9)$$

$$\frac{I_{single-phase}(t)}{I_{single-phase}(0)} = \frac{R(\theta(t)) e^{-2M(t)} c(t)}{R(\theta(0)) e^{-2M(0)} c(0)} \quad (10)$$

$$\frac{c(t)}{c(0)} = \frac{I_{single-phase}(t) R(\theta(0))}{I_{single-phase}(0) R(\theta(t))} e^{-2(M(0)-M(t))} \quad (11)$$

At a specific temperature, all factors that affect the peak intensity (Lorentz–polarization, structure, multiplicity, absorption, and temperature factors) tend to be similar, independently of the exposure time at those temperatures. However, considering the phase transformation and precipitates dissolution during the PDHTs, slight changes in 2θ (affecting the Lorentz–polarization) can occur due to the phase evolution, change in composition, and morphology, as reported by Idell et al. [76] and Stoudt et al. [72] for Inconel® 625 fabricated via PBF. In addition, the multiplicity factor (p) is a function of the unit cell and does not change for a single-phase peak during the heat treatment. The structure factor ($F |hkl|^2$) is independent of the phase unit cell shape and size, implying that despite possible unit cell alteration (e.g., change in lattice parameters due to diffusion), atoms' positions (atomic scattering factor) will be similar, i.e., $F |hkl|^2$ can also be considered constant during the PDHT [49]. In relation to v (unit cell volume), Lindwall et al. [69] and Zhang et al. [75] (both Inconel® 625 fabricated via PBF) considered this variable constant during the heat treatment. They [69,75] obtained a good match between the secondary phase content estimated via image analysis and SXRD, which indicated that v does not significantly change during the PDHT and can also be considered a constant parameter. The analysis described above indicated that $\frac{R(\theta)}{R(\theta_0)}$ (Eq. 8) depends only on the Lorentz–polarization factor (i.e., 2θ). In addition, as exemplified for the δ phase (Fig. 13a), the Lorentz–polarization factor was not significantly (almost constant, $\cong 1$) affected during the heat treatment. A similar analysis was also performed for the temperature factor (e^{-2M}), which also showed be independent of the time during the PDHT (Fig. 13b). Thus, the relative phase content, $\frac{c(t)}{c(0)}$, can be expressed by Equation 12. For a better description of the SXRD data analysis and temperature factor, see [Supplementary material](#).

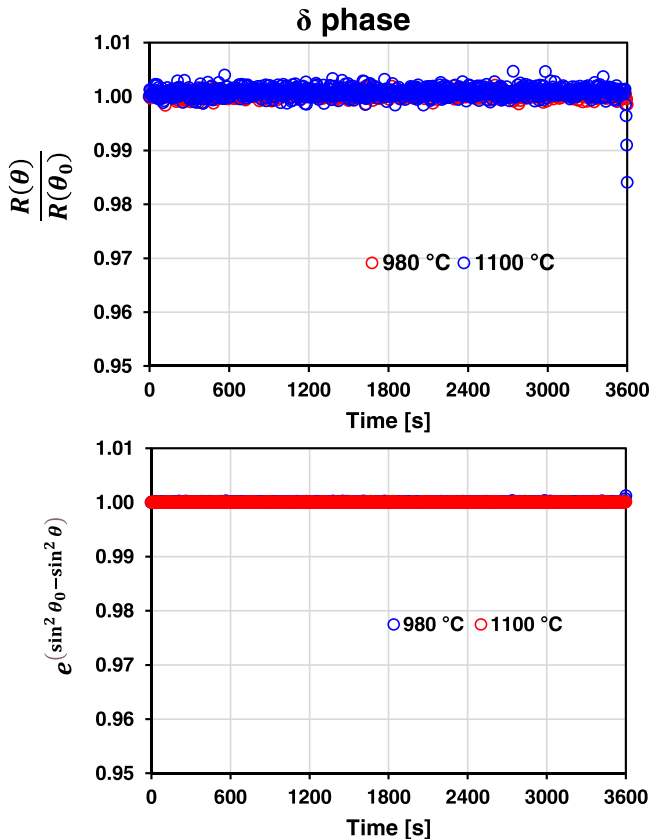


Fig. 13. Normalized Lorentz–polarization ($\frac{R(\theta)}{R(\theta_0)}$) and temperature ($e^{(\sin^2\theta_0 - \sin^2\theta)}$) factors variation during the post-deposition heat treatment.

$$\frac{c(t)}{c(0)} = \frac{I_{\text{single-phase}}(t)}{I_{\text{single-phase}}(0)} \quad (12)$$

After about 1200 s of the solution PDHT soaking time, where chemical composition homogenization by diffusion is expected to be more notorious [72], secondary phases become unstable and start to dissolve, resulting in peak intensity reduction (Fig. 11d and Fig. 11e). However, the remaining time is insufficient to completely dissolve them, suggesting that longer soaking times or higher peak temperatures than that indicated in the material specification (ASTM B 446) are required for Inconel® 625 fabricated via arc plasma DED. Floreen et al. [80], wrought Inconel® 625, highlighted that the complete secondary phase dissolution could be achieved using long soaking times (24 h) at 1100 °C, reinforcing the present results. Idell et al. [76] and Stoudt et al. [72], Inconel® 718Plus and 625 fabricated via PBF, respectively, reported that δ phase could form during the entire isothermal annealing (1066 °C/1 h), attributing this to the high interdendritic microsegregation (especially Nb and Mo as also showed in Fig. 12b), which increase both the stable temperature range and precipitation kinetics ($\sim 10^{1-2}$ times) in relation to the wrought material. Zhang et al. [77] and Shankar et al. [83], Inconel® 625 fabricated via PBF and hot rolling Inconel® 625, respectively, showed that a higher peak temperature (1150 °C/1 h) can homogenize the composition and dissolve the majority of secondary phases. In addition, it is worth mentioning the difference in dissolution/precipitation kinetics between the dendritic core and interdendritic regions expressed by the TTT diagram (Fig. 12c). For interdendritic regions, the precipitation and partial dissolution of deleterious phases during the stabilization and solution PDHTs, respectively, were correctly predicted and supported by the SXRD results and literature [72,76,77,80,83].

The δ phase is pointed out as a grain growth suppressor via the Zener pinning effect [78,84,85], which can be related to the FWHM plateau (stabilization PDHT – δ sub-solvus temperature; Fig. 8), i.e., δ hidden the peak broadening source density reduction by pinning the high-angle mobile grain boundaries [86]. Additionally, despite the present work be focused on Inconel® 625 fabricated via in situ interlayer hot forging arc plasma DED, the presented Laves and δ phases evolution (Fig. 11) can be extended to arc plasma DED, which is corroborated by previous literature results [5,6,45,69,71,72,75–78]. Thus, low peak temperature PDHT drives the secondary phase precipitation, while high peak temperature enables more homogenous chemical composition and lower content of secondary phases. The present SXRD results and those of Lass et al. [79] (Inconel® 625 fabricated via PBF) indicate that longer solution PDHT soaking times (> 1 h) could drive the complete dissolution of preexisting secondary phases. In addition, as highlighted by Xi et al. [40] and Luna et al. [87], the use of higher peak temperatures (1185 and 1177 °C/ 1 h, respectively) can almost completely dissolve Laves and δ phases. However, considering that the in situ interlayer hot forging grain size refinement primarily occurs by static recrystallization, longer soaking times or higher peak temperatures must be carefully analyzed to avoid abnormal grain growth, which can neutralize the in situ interlayer hot forging grain size refinement effect.

4. Conclusions

The present work demonstrated that the combined use of in situ interlayer hot forging with PDHT drove a finer and less oriented microstructure on the Ni-based superalloy 625 obtained by arc plasma DED. Solution (1100 °C/1 h) PDHT had a better response, enabling a finer grain size and less oriented microstructure than stabilization (980 °C/1 h) PDHT. *In situ* SRXD, supported by the thermodynamic simulations, evidenced that the solution PDHT partially dissolved the secondary phases (Laves and δ). In contrast,

stabilization PDHT induced their precipitation in the interdendritic regions. Also, the dislocation density evolution indicated that in situ interlayer hot forging generated enough crystal defects to promote grain size refinement via static recrystallization during PDHT, meeting the AMS 5662 grain size requirement.

CRedit authorship contribution statement

Francisco Werley Cipriano Farias – Conceptualization, Data curation, Formal analysis, Investigation, Methodology, Validation, Writing – original draft. **Valdemar R. Duarte** – Conceptualization, Data curation, Formal analysis, Investigation, Methodology, Supervision, Writing – review & editing. **Igor Oliveira Felice** – Formal analysis, Investigation, Writing – review & editing. **João da Cruz Payão Filho** – Software, Validation. **Norbert Schell** – Investigation, Resources. **Emad Maawad** – Investigation. **J. Y. Li** – Data curation, Investigation. **Y. Zhang** – Data curation, Investigation. **T.G. Santos** – Conceptualization, Data curation, Formal analysis, Funding acquisition, Investigation, Methodology, Project administration, Resources, Supervision, Visualization, Writing – review & editing. **J. P. Oliveira** – Conceptualization, Data curation, Formal analysis, Funding acquisition, Investigation, Methodology, Project administration, Resources, Supervision, Visualization, Writing – review & editing.

Data Availability

The authors do not have permission to share data.

Declaration of Competing Interest

The authors declare that they have no known competing financial interests or personal relationships that could have appeared to influence the work reported in this paper.

Acknowledgments

Authors acknowledge the Portuguese Fundação para a Ciência e a Tecnologia (FCT – MCTES) for its financial support via the project UID/EMS/00667/2019 (UNIDEMI). JPO acknowledges funding by national funds from FCT - Fundação para a Ciência e a Tecnologia, I.P., in the scope of the projects LA/P/0037/2020, UIDP/50025/2020 and UIDB/50025/2020 of the Associate Laboratory Institute of Nanostructures, Nanomodelling and Nanofabrication – i3N. Funding of CENIMAT/i3N by national funds through the FCT-Fundação para a Ciência e a Tecnologia, I.P., within the scope of Multiannual Financing of R&D Units, reference UIDB/50025/2020–2023 is also acknowledge. FWCF acknowledges Fundação para a Ciência e a Tecnologia (FCT-MCTES) for funding the Ph.D. Grant 2022.13870. BD. The authors acknowledge DESY (Hamburg, Germany), a member of the Helmholtz Association HGF, for the provision of experimental facilities. Beamtime was allocated for proposal I-20210986 EC. The research leading to this result has been supported by the project CALIPSOplus under the Grant Agreement 730872 from the EU Framework Programme for Research and Innovation HORIZON 2020. This activity has received funding from the European Institute of Innovation and Technology (EIT) Raw Materials through the project Smart WAAM: Microstructural Engineering and Integrated Non-Destructive Testing. YZ acknowledges the National Natural Science Foundation of China (51601091), the Natural Science Foundation of Jiangsu Province (BK 20160826), the Six Talent Peaks Project of Jiangsu Province (2017-XCL-051), the Fundamental Research Funds for the Central Universities (30917011106), and Key Research and Development Plan of Jiangsu Province (BE 2020085).

Appendix A. Supporting information

Supplementary data associated with this article can be found in the online version at [doi:10.1016/j.jallcom.2023.170059](https://doi.org/10.1016/j.jallcom.2023.170059).

References

- [1] A. Gamon, E. Arrieta, P.R. Gradl, C. Katsarelis, L.E. Murr, R.B. Wicker, F. Medina, Microstructure and hardness comparison of as-built Inconel 625 alloy following various additive manufacturing processes, *Results Mater.* 12 (2021) 100239, <https://doi.org/10.1016/j.rinma.2021.100239>
- [2] A. Chintala, M. Tejaswi Kumar, M. Sathishkumar, N. Arivazhagan, M. Manikandan, Technology development for producing Inconel 625 in aerospace application using wire arc additive manufacturing process, *J. Mater. Eng. Perform.* 30 (2021) 5333–5341, <https://doi.org/10.1007/s11665-021-05781-6>
- [3] W. Yangfan, C. Xizhang, S. Chuanchu, Microstructure and mechanical properties of Inconel 625 fabricated by wire-arc additive manufacturing, *Surf. Coat. Technol.* 374 (2019) 116–123, <https://doi.org/10.1016/j.surfcoat.2019.05.079>
- [4] S. Li, J.Y. Li, Z.W. Jiang, Y. Cheng, Y.Z. Li, S. Tang, J.Z. Leng, H.X. Chen, Y. Zou, Y.H. Zhao, J.P. Oliveira, Y. Zhang, K.H. Wang, Controlling the columnar-to-equiaxed transition during directed energy deposition of Inconel 625, *Addit. Manuf.* 57 (2022) 102958, <https://doi.org/10.1016/j.addma.2022.102958>
- [5] A.N.M. Tanvir, M.R.U. Ahsan, G. Seo, J. duk Kim, C. Ji, B. Bates, Y. Lee, D.B. Kim, Heat treatment effects on Inconel 625 components fabricated by wire + arc additively manufacturing (WAAM)—part 2: mechanical properties, *Int. J. Adv. Manuf. Technol.* 110 (2020) 1709–1721, <https://doi.org/10.1007/s00170-020-05980-w>
- [6] A.N.M. Tanvir, M.R.U. Ahsan, C. Ji, W. Hawkins, B. Bates, Duck, B. Kim, Heat treatment effects on Inconel 625 components fabricated by wire + arc additive manufacturing (WAAM)—part 1: microstructural characterization, *Int. J. Adv. Manuf. Technol.* 103 (2019) 3785–3798, <https://doi.org/10.1007/s00170-019-03828-6>
- [7] Q. Jiang, P. Zhang, Z. Yu, H. Shi, S. Li, D. Wu, H. Yan, X. Ye, J. Chen, Microstructure and mechanical properties of thick-walled Inconel 625 alloy manufactured by wire arc additive manufacture with different torch paths, *Adv. Eng. Mater.* 23 (2021) 2000728, <https://doi.org/10.1002/ADEM.202000728>
- [8] Y. Wang, X. Chen, Investigation on the microstructure and corrosion properties of Inconel 625 alloy fabricated by wire arc additive manufacturing, *Mater. Res. Express* 6 (2019) 106568, <https://doi.org/10.1088/2053-1591/ab39f6>
- [9] A. Banerjee, S. Messina, M.R. Begley, E.J. Schwalbach, M.A. Groeber, W.D. Musinski, P.A. Shade, M.E. Cox, J.D. Miller, K.J. Hemker, The mechanical response of additively manufactured IN625 thin-walled structures, *Scr. Mater.* 205 (2021) 114188, <https://doi.org/10.1016/j.scriptamat.2021.114188>
- [10] T.A. Rodrigues, V.R. Duarte, D. Tomás, J.A. Avila, J.D. Escobar, E. Rossinyol, N. Schell, T.G. Santos, J.P. Oliveira, In-situ strengthening of a high strength low alloy steel during wire and arc additive manufacturing (WAAM), *Addit. Manuf.* 34 (2020) 101200, <https://doi.org/10.1016/j.addma.2020.101200>
- [11] Y. Chen, M. Xu, T. Zhang, J. Xie, K. Wei, S. Wang, L. Yin, P. He, Grain refinement and mechanical properties improvement of Inconel 625 alloy fabricated by ultrasonic-assisted wire and arc additive manufacturing, *J. Alloy. Compd.* 910 (2022) 164957, <https://doi.org/10.1016/j.jallcom.2022.164957>
- [12] F.W.C. Farias, J. da, C. Payão Filho, V.H.P. Moraes e Oliveira, Prediction of the interpass temperature of a wire arc additive manufactured wall: FEM simulations and artificial neural network, *Addit. Manuf.* 48 (2021) 102387, <https://doi.org/10.1016/j.addma.2021.102387>
- [13] Y. Wang, X. Chen, Q. Shen, C. Su, Y. Zhang, S. Jayalakshmi, R.A. Singh, Effect of magnetic field on the microstructure and mechanical properties of Inconel 625 superalloy fabricated by wire arc additive manufacturing, *J. Manuf. Process* 64 (2021) 10–19, <https://doi.org/10.1016/j.jmapro.2021.01.008>
- [14] V.R. Duarte, T.A. Rodrigues, N. Schell, R.M. Miranda, J.P. Oliveira, T.G. Santos, In-situ hot forging direct energy deposition-arc of CuAl8 alloy, *Addit. Manuf.* (2022) 102847, <https://doi.org/10.1016/j.addma.2022.102847>
- [15] X. Xu, S. Ganguly, J. Ding, C.E. Seow, S. Williams, Enhancing mechanical properties of wire + arc additively manufactured INCONEL 718 superalloy through in-process thermomechanical processing, *Mater. Des.* 160 (2018) 1042–1051, <https://doi.org/10.1016/j.matdes.2018.10.038>
- [16] P.A. Colegrove, J. Donoghue, F. Martina, J. Gu, P. Prangnell, J. Hönnige, Application of bulk deformation methods for microstructural and material property improvement and residual stress and distortion control in additively manufactured components, *Scr. Mater.* 135 (2017) 111–118, <https://doi.org/10.1016/j.scriptamat.2016.10.031>
- [17] C. Liu, J. Yang, Q. Ge, F. Gao, J. Zou, Mechanical properties improvement of thick multi-pass weld by layered ultrasonic impact treatment, *Sci. Technol. Weld. Join.* 23 (2018) 95–104, <https://doi.org/10.1080/13621718.2017.1327201>
- [18] T.E. Adams, S. Härtel, A. Hälsig, B. Awiszus, P. Mayr, WeldForming: a new inline process combination to improve weld seam properties, *Weld. World* 64 (2020) 601–610, <https://doi.org/10.1007/s40194-020-00856-9>
- [19] W. Liu, X. Tian, X. Zhang, Preventing weld hot cracking by synchronous rolling during welding, *Weld. J.* 75 (1996) 297s–304s.
- [20] H.E. Coules, P. Colegrove, L.D. Cozzolino, S.W. Wen, S. Ganguly, T. Pirling, Effect of high pressure rolling on weld-induced residual stresses, *Sci. Technol. Weld. Join.* 17 (2012) 394–401, <https://doi.org/10.1179/1362171812Y.0000000021>
- [21] F. Martina, M.J. Roy, B.A. Szost, S. Terzi, P.A. Colegrove, S.W. Williams, P.J. Withers, J. Meyer, M. Hofmann, Residual stress of as-deposited and rolled wire+arc

- additive manufacturing Ti-6Al-4V components, *Mater. Sci. Technol.* 32 (2016) 1439–1448, <https://doi.org/10.1080/02670836.2016.1142704>
- [22] J. Chen, H. Wei, X. Zhang, Y. Peng, J. Kong, K. Wang, Flow behavior and microstructure evolution during dynamic deformation of 316 L stainless steel fabricated by wire and arc additive manufacturing, *Mater. Des.* 198 (2021) 109325, <https://doi.org/10.1016/j.matdes.2020.109325>
- [23] B. Lan, Y. Wang, Y. Liu, P. Hooper, C. Hopper, G. Zhang, X. Zhang, J. Jiang, The influence of microstructural anisotropy on the hot deformation of wire arc additive manufactured (WAAM) Inconel 718, *Mater. Sci. Eng. A* 823 (2021) 141733, <https://doi.org/10.1016/j.msea.2021.141733>
- [24] B. Liu, Y. Ding, J. Xu, Y. Gao, X. Wang, H. Zhang, Y. Hu, F. Sun, Outstanding strength-ductility synergy in Inconel 718 superalloy via laser powder bed fusion and thermomechanical treatment, *Addit. Manuf.* 67 (2023) 103491, <https://doi.org/10.1016/j.addma.2023.103491>
- [25] Y. Zhou, X. Lin, N. Kang, Z. Wang, H. Tan, W. Huang, Hot deformation induced microstructural evolution in local-heterogeneous wire + arc additive manufactured 2219 Al alloy, *J. Alloy. Compd.* 865 (2021) 158949, <https://doi.org/10.1016/j.jallcom.2021.158949>
- [26] W. Zhao, G.C. Zha, M.Z. Xi, S.Y. Gao, Effects of synchronous rolling on microstructure, hardness, and wear resistance of laser multilayer cladding, *J. Mater. Eng. Perform.* 27 (2018) 1746–1752, <https://doi.org/10.1007/s11665-018-3286-x>
- [27] Q. Li, Y. Zhang, J. Chen, B. Guo, W. Wang, Y. Jing, Y. Liu, Effect of ultrasonic micro-forging treatment on microstructure and mechanical properties of GH3039 superalloy processed by directed energy deposition, *J. Mater. Sci. Technol.* 70 (2021) 185–196, <https://doi.org/10.1016/j.jmst.2020.09.001>
- [28] T. Zhang, H. Li, H. Gong, J. Ding, Y. Wu, C. Diao, X. Zhang, S. Williams, Hybrid wire – arc additive manufacture and effect of rolling process on microstructure and tensile properties of Inconel 718, *J. Mater. Process. Technol.* 299 (2022) 117361, <https://doi.org/10.1016/j.jmatprotec.2021.117361>
- [29] C. Li, Y. Tian, Y. Chen, P. Hodgson, X. Wu, Y. Zhu, A. Huang, Hierarchical layered and refined grain structure of Inconel 718 superalloy produced by rolling-assisted directed energy deposition, *Addit. Manuf. Lett.* 1 (2021) 100009, <https://doi.org/10.1016/j.addlet.2021.100009>
- [30] Q. Chen, G. Wang, H. Zhang, R. Li, Research on microstructure and mechanical properties of hybrid plasma arc and micro-rolling additive manufacturing of Inconel 718 superalloy, *Rapid Prototyp. J.* 28 (2022) 1509–1519, <https://doi.org/10.1108/rpj-09-2021-0227>
- [31] F.W.C. Farias, V.R. Duarte, I.O. Felice, J. da, C.P. Filho, N. Schell, E. Maawad, J.A. Avila, J.Y. Li, Y. Zhang, T.G. Santos, J.P. Oliveira, In situ interlayer hot forging arc-based directed energy deposition of Inconel® 625: process development and microstructure effects, *Addit. Manuf.* 66 (2023) 103476, <https://doi.org/10.1016/j.addma.2023.103476>
- [32] J.R. Hönnige, A.E. Davis, A. Ho, J.R. Kennedy, L. Neto, P. Prangnell, S. Williams, The effectiveness of grain refinement by machine hammer peening in high deposition rate wire-arc AM Ti-6Al-4V, *Metall. Mater. Trans. A* 51 (2020) 3692–3703, <https://doi.org/10.1007/s11661-020-05781-6>
- [33] V.R. Duarte, T.A. Rodrigues, N. Schell, R.M. Miranda, J.P. Oliveira, T.G. Santos, Hot forging wire and arc additive manufacturing (HF-WAAM), *Addit. Manuf.* 35 (2020) 101193, <https://doi.org/10.1016/j.addma.2020.101193>
- [34] A.P. Hammersley, FIT2D: a multi-purpose data reduction, analysis and visualization program, *J. Appl. Crystallogr.* 49 (2016) 646–652, <https://doi.org/10.1107/S1600576716000045>
- [35] T.A. Rodrigues, J.D. Escobar, J. Shen, V.R. Duarte, G.G. Ribamar, J.A. Avila, E. Maawad, N. Schell, T.G. Santos, J.P. Oliveira, Effect of heat treatments on 316 stainless steel parts fabricated by wire and arc additive manufacturing: microstructure and synchrotron X-ray diffraction analysis, *Addit. Manuf.* 48 (2021) 102428, <https://doi.org/10.1016/j.addma.2021.102428>
- [36] T.A. Rodrigues, F.W.C. Farias, J.A. Avila, E. Maawad, N. Schell, T.G. Santos, J.P. Oliveira, Effect of heat treatments on Inconel 625 fabricated by wire and arc additive manufacturing: an in situ synchrotron X-ray diffraction analysis, *Sci. Technol. Weld. Join.* (2023) 1–6, <https://doi.org/10.1080/13621718.2023.2187927>
- [37] F. Bachmann, R. Hielscher, H. Schaeßen, Texture analysis with MTEX – free and open source software toolbox, *Solid State Phenom.* 160 (2010) 63–68, <https://doi.org/10.4028/www.scientific.net/SSP.160.63>
- [38] N. Pepe, S. Egerland, P.A. Colegrove, D. Yapp, A. Leonhartsberger, A. Scotti, Measuring the process efficiency of controlled gas metal arc welding processes, *Sci. Technol. Weld. Join.* 16 (2011) 412–417, <https://doi.org/10.1179/1362171810Y.0000000029>
- [39] Y. Wang, J. Shi, Recrystallization behavior and tensile properties of laser metal deposited Inconel 718 upon in-situ ultrasonic impact peening and heat treatment, *Mater. Sci. Eng. A* 786 (2020) 139434, <https://doi.org/10.1016/j.msea.2020.139434>
- [40] N. Xi, X. Fang, Y. Duan, Q. Zhang, K. Huang, Wire arc additive manufacturing of Inconel 718: Constitutive modelling and its microstructure basis, *J. Manuf. Process.* 75 (2022) 1134–1143, <https://doi.org/10.1016/j.jmapro.2022.01.067>
- [41] A. Safarzade, M. Sharifitabar, M.A. Shafiee, Effects of heat treatment on microstructure and mechanical properties of Inconel 625 alloy fabricated by wire arc additive manufacturing process, *Trans. Nonferrous Met. Soc. China* 30 (2020) 3016–3030, [https://doi.org/10.1016/S1003-6326\(20\)65439-5](https://doi.org/10.1016/S1003-6326(20)65439-5)
- [42] G. Ravi, N. Murugan, R. Arulmani, Microstructure and mechanical properties of Inconel-625 slab component fabricated by wire arc additive manufacturing, *Mater. Sci. Technol.* 36 (2020) 1785–1795, <https://doi.org/10.1080/02670836.2020.1836737>
- [43] Y.L. Hu, X. Lin, S.Y. Zhang, Y.M. Jiang, X.F. Lu, H.O. Yang, W.D. Huang, Effect of solution heat treatment on the microstructure and mechanical properties of Inconel 625 superalloy fabricated by laser solid forming, *J. Alloy. Compd.* 767 (2018) 330–344, <https://doi.org/10.1016/j.jallcom.2018.07.087>
- [44] Y. Hu, X. Lin, Y. Li, S. Zhang, Q. Zhang, W. Chen, W. Li, W. Huang, Influence of heat treatments on the microstructure and mechanical properties of Inconel 625 fabricated by directed energy deposition, *Mater. Sci. Eng. A* 817 (2021) 141309, <https://doi.org/10.1016/j.msea.2021.141309>
- [45] C.E. Seow, H.E. Coules, G. Wu, R.H.U. Khan, X. Xu, S. Williams, Wire + Arc additively manufactured Inconel 718: effect of post-deposition heat treatments on microstructure and tensile properties, *Mater. Des.* 183 (2019) 108157, <https://doi.org/10.1016/j.matdes.2019.108157>
- [46] M. Gustafsson, M. Thuvander, E.L. Bergqvist, E. Keehan, L. Karlsson, Effect of welding procedure on texture and strength of nickel based weld metal, *Sci. Technol. Weld. Join.* 12 (2013) 549–555, <https://doi.org/10.1179/174329307x213800>
- [47] R.J. Moat, A.J. Pinkerton, L. Li, P.J. Withers, M. Preuss, Crystallographic texture and microstructure of pulsed diode laser-deposited Waspaloy, *Acta Mater.* 57 (2009) 1220–1229, <https://doi.org/10.1016/j.actamat.2008.11.004>
- [48] H.J. Bunge, *Texture Analysis in Materials Science*, Elsevier, 1982, <https://doi.org/10.1016/C2013-0-11769-2>
- [49] B.D. Cullity, S.R. Stock, *Elements of X-Ray Diffraction*, third ed., Pearson Education Limited, 2014.
- [50] S. Das Bakshi, D. Sinha, S. Ghosh Chowdhury, Anisotropic broadening of XRD peaks of α -Fe: Williamson-Hall and Warren-Averbach analysis using full width at half maximum (FWHM) and integral breadth (IB), *Mater. Charact.* 142 (2018) 144–153, <https://doi.org/10.1016/j.matchar.2018.05.018>
- [51] J. Hönnige, C.E. Seow, S. Ganguly, X. Xu, S. Cabeza, H. Coules, S. Williams, Study of residual stress and microstructural evolution in as-deposited and inter-pass rolled wire plus arc additively manufactured Inconel 718 alloy after ageing treatment, *Mater. Sci. Eng. A* 801 (2021), <https://doi.org/10.1016/j.msea.2020.140368>
- [52] M. Moreno, J. Teixeira, G. Geandier, J.C. Hell, F. Bonnet, M. Salib, S.Y.P. Allain, Real-time investigation of recovery, recrystallization and austenite transformation during annealing of a cold-rolled steel using high energy X-ray diffraction (HEXRD), *Metals* 9 (2018) 8, <https://doi.org/10.3390/MET9010008>
- [53] X. Liu, J. Fan, K. Li, Y. Song, D. Liu, R. Yuan, J. Wang, B. Tang, H. Kou, J. Li, Serrated flow behavior and microstructure evolution of Inconel 625 superalloy during plane-strain compression with different strain rates, *J. Alloy. Compd.* 881 (2021) 160648, <https://doi.org/10.1016/j.jallcom.2021.160648>
- [54] J. Čapek, E. Polatidis, M. Knapik, C. Lyphout, N. Casati, R. Pederson, M. Strobl, The effect of γ and δ phase precipitation on the mechanical properties of Inconel 718 manufactured by selective laser melting: an in situ neutron diffraction and acoustic emission study, *JOM* 73 (2021) 223–232, <https://doi.org/10.1007/s11837-020-04463-3>
- [55] Y. Wang, Z. Jia, J. Ji, S. Li, D. Liu, Evolution of stacking fault and dislocation during dynamic recrystallization of Inconel 625 alloy, *Adv. Eng. Mater.* 24 (2022) 2200657, <https://doi.org/10.1002/ADEM.202200657>
- [56] D. Hull, D.J. Bacon, *Introduction to Dislocations*, fifth ed., Elsevier Ltd, 2011, <https://doi.org/10.1016/C2009-0-64358-0>
- [57] A.S. Argon, W.C. Moffatt, Climb of extended edge dislocations, *Acta Met.* 29 (1981) 293–299, [https://doi.org/10.1016/0001-6160\(81\)90156-5](https://doi.org/10.1016/0001-6160(81)90156-5)
- [58] G.K. Williamson, W.H. Hall, X-ray line broadening from filed aluminium and wolfram, *Acta Met.* 1 (1953) 22–31, [https://doi.org/10.1016/0001-6160\(53\)90006-6](https://doi.org/10.1016/0001-6160(53)90006-6)
- [59] R.E. Smallman, K.H. Westmacott, Stacking faults in face-centred cubic metals and alloys, *Philos. Mag. A* J. Theor. Exp. Appl. Phys. 2 (2010) 669–683, <https://doi.org/10.1080/14786435708242709>
- [60] A. Borbély, The modified Williamson-Hall plot and dislocation density evaluation from diffraction peaks, *Scr. Mater.* 217 (2022) 114768, <https://doi.org/10.1016/j.scriptamat.2022.114768>
- [61] S.K. Rai, A. Kumar, V. Shankar, T. Jayakumar, K.B.S. Rao, B. Raj, Characterization of microstructures in Inconel 625 using X-ray diffraction peak broadening and lattice parameter measurements, *Scr. Mater.* 51 (2004) 59–63, <https://doi.org/10.1016/j.scriptamat.2004.03.017>
- [62] C. Li, P. Hodgson, M. Preuss, Y. Chen, X. Wu, Y. Zhu, Y. Tian, A. Huang, Rolling-assisted direct energy deposited Inconel 718: Microstructural evolution and mechanical properties after optimized heat treatment, *J. Mater. Sci. Technol.* 144 (2023) 118–127, <https://doi.org/10.1016/j.jmst.2022.10.021>
- [63] T. De Terris, P. Peyre, O. Castelnaud, Z. Hadjem-Hamouche, H. Haddadi, V. Michel, Analysis of As-built microstructures and recrystallization phenomena on inconel 625 alloy obtained via laser powder bed fusion (L-PBF), *Metals (Basel)* 11 (2021) 619–641, <https://doi.org/10.3390/MET11040619>
- [64] K. Huang, R.E. Logé, A review of dynamic recrystallization phenomena in metallic materials, *Mater. Des.* 111 (2016) 548–574, <https://doi.org/10.1016/j.matdes.2016.09.012>
- [65] A. Rollett, F.J. Humphreys, G.S. Rohrer, M. Hatherly, A. Rollett, *Recrystallization and Related Annealing Phenomena*, second ed., Elsevier Ltd, 2017, <https://doi.org/10.1016/B978-0-08-098235-9.00001-X>
- [66] F. Schmeiser, E. Krohmer, C. Wagner, N. Schell, E. Uhlmann, W. Reimers, In situ microstructure analysis of Inconel 625 during laser powder bed fusion, *J. Mater. Sci.* 57 (2021) 9663–9677, <https://doi.org/10.1007/s10853-021-06577-8>
- [67] K. Prasad, Y. Horita, A. Ito, S. Torizuka, In situ synchrotron diffraction study of a crack-free additively manufactured Ni base superalloy, *Scr. Mater.* 200 (2021) 113896, <https://doi.org/10.1016/j.scriptamat.2021.113896>
- [68] J.N. DuPont, C.V. Robino, J.R. Michael, M.R. Nours, A.R. Marder, Solidification of Nb-bearing superalloys: Part I. Reaction sequences, *Mater. Trans.* A 29 (1998) 2785–2796, <https://doi.org/10.1007/S11661-998-0319-3>

- [69] G. Lindwall, C.E. Campbell, E.A. Lass, F. Zhang, M.R. Stoudt, A.J. Allen, L.E. Levine, Simulation of TTT curves for additively manufactured Inconel 625, *Metall. Mater. Trans. A* 50 (2019) 457–467, <https://doi.org/10.1007/s11661-018-4959-7>
- [70] S.A. Oh, R.E. Lim, J.W. Aroh, A.C. Chuang, B.J. Gould, J.V. Bernier, N. Parab, T. Sun, R.M. Suter, A.D. Rollett, Microscale observation via high-speed X-ray diffraction of alloy 718 during in situ laser melting, *JOM* 73 (2021) 212–222, <https://doi.org/10.1007/s11837-020-04481-1>
- [71] D. Van, G.P. Dinda, J. Park, J. Mazumder, S.H. Lee, Enhancing hardness of Inconel 718 deposits using the aging effects of cold metal transfer-based additive manufacturing, *Mater. Sci. Eng. A* 776 (2020) 139005, <https://doi.org/10.1016/j.msea.2020.139005>
- [72] M.R. Stoudt, E.A. Lass, D.S. Ng, M.E. Williams, F. Zhang, C.E. Campbell, G. Lindwall, L.E. Levine, The influence of annealing temperature and time on the formation of δ -phase in additively-manufactured inconel 625, *Metall. Mater. Trans. A* 49 (2018) 3028–3037, <https://doi.org/10.1007/s11661-018-4643-y>
- [73] M.J. Cieslak, T.J. Headley, T. Kollie, A.D. Romig, A melting and solidification study of alloy 625, *Metall. Trans. A* 19 (1988) 2319–2331, <https://doi.org/10.1007/BF02645056>
- [74] M.J. Cieslak, The welding and solidification metallurgy of alloy 625, *Weld. J.* (1991) 49s–56s.
- [75] F. Zhang, L.E. Levine, A.J. Allen, M.R. Stoudt, G. Lindwall, E.A. Lass, M.E. Williams, Y. Idell, C.E. Campbell, Effect of heat treatment on the microstructural evolution of a nickel-based superalloy additive-manufactured by laser powder bed fusion, *Acta Mater.* 152 (2018) 200–214, <https://doi.org/10.1016/j.actamat.2018.03.017>
- [76] Y. Idell, L.E. Levine, A.J. Allen, F. Zhang, C.E. Campbell, G.B. Olson, J. Gong, D.R. Snyder, H.Z. Deutchman, Unexpected δ -phase formation in additive-manufactured Ni-based superalloy, *JOM* 68 (2016) 950–959, <https://doi.org/10.1007/s11837-015-1772-2>
- [77] F. Zhang, L.E. Levine, A.J. Allen, C.E. Campbell, E.A. Lass, S. Cheruvathur, M.R. Stoudt, M.E. Williams, Y. Idell, Homogenization kinetics of a nickel-based superalloy produced by powder bed fusion laser sintering, *Scr. Mater.* 131 (2017) 98–102, <https://doi.org/10.1016/j.scriptamat.2016.12.037>
- [78] C. Li, R. White, X.Y. Fang, M. Weaver, Y.B. Guo, Microstructure evolution characteristics of Inconel 625 alloy from selective laser melting to heat treatment, *Mater. Sci. Eng. A* 705 (2017) 20–31, <https://doi.org/10.1016/j.msea.2017.08.058>
- [79] E.A. Lass, M.R. Stoudt, M.E. Williams, M.B. Katz, L.E. Levine, T.Q. Phan, T.H. Gnaeupel-Herold, D.S. Ng, Formation of the Ni3Nb δ -phase in stress-relieved inconel 625 produced via laser powder-bed fusion additive manufacturing, *Metall. Mater. Trans. A* 48 (2017) 5547–5558, <https://doi.org/10.1007/S11661-017-4304-6>
- [80] S. Floreen, G.E. Fuchs, W.J. Yang, The Metallurgy of Alloy 625, in: E.A. Loria (Ed.), *Superalloys 718, 625, 706 Var. Deriv.*, 1994: pp. 13–37. <https://www.tms.org/superalloys/> (accessed December 26, 2022).
- [81] T. Antonsson, H. Fredriksson, The effect of cooling rate on the solidification of INCONEL 718, *Metall. Mater. Trans. B* 36 (2005) 85–96, <https://doi.org/10.1007/S11663-005-0009-0>
- [82] L.H.M. Antunes, M. Bé Reš, J.J. Hoyos, L. Novotný, N. Novotný, H.F.G. De Abreu, P.F. Da, S. Farina, Kinetics of FCC to HCP transformation during aging heat treatment of Co–28Cr–6Mo alloy fabricated by laser-powder bed fusion, *Metall. Mater. Trans. A* (2023) 1–11, <https://doi.org/10.1007/s11661-023-07016-w>
- [83] V. Shankar, K. Bhanu Sankara Rao, S.L. Mannan, Microstructure and mechanical properties of Inconel 625 superalloy, *J. Nucl. Mater.* 288 (2001) 222–232, [https://doi.org/10.1016/S0022-3115\(00\)00723-6](https://doi.org/10.1016/S0022-3115(00)00723-6)
- [84] Y. Wang, W.Z. Shao, L. Zhen, B.Y. Zhang, Hot deformation behavior of delta-processed superalloy 718, *Mater. Sci. Eng. A* 528 (2011) 3218–3227, <https://doi.org/10.1016/j.msea.2011.01.013>
- [85] M.A.R. Medeiros, C.H. de Melo, A.L. Pinto, L.H. de Almeida, L.S. Araújo, The δ phase precipitation during processing and the influence on grain boundary character distribution and mechanical properties of superalloy 718, *Mater. Sci. Eng. A* 726 (2018) 187–193, <https://doi.org/10.1016/j.msea.2018.04.073>
- [86] Y.C. Lin, D.G. He, M.S. Chen, X.M. Chen, C.Y. Zhao, X. Ma, Z.L. Long, EBSD analysis of evolution of dynamic recrystallization grains and δ phase in a nickel-based superalloy during hot compressive deformation, *Mater. Des.* 97 (2016) 13–24, <https://doi.org/10.1016/j.matdes.2016.02.052>
- [87] V. Luna, H. Wang, J. Fuh, L. Trujillo, A. Gamon, E. Arrieta, L.E. Murr, R.B. Wicker, C. Katsarelis, P.R. Gradl, F. Medina, Comprehensive and comparative heat treatment of additively manufactured inconel 625 alloy and corresponding microstructures and mechanical properties, *J. Manuf. Mater. Process.* 6 (2022) 107, <https://doi.org/10.3390/jmmp6050107>